Science Advances

AAAS

advances.sciencemag.org/cgi/content/full/3/4/e1601939/DC1

Supplementary Materials for

Design and function of biomimetic multilayer water purification membranes

Shengjie Ling, Zhao Qin, Wenwen Huang, Sufeng Cao, David L. Kaplan, Markus J. Buehler

Published 5 April 2017, *Sci. Adv.* **3**, e1601939 (2017)
DOI: 10.1126/sciadv.1601939

The PDF file includes:

- table S2. Numerical values of the physical parameters of the five coarse-grained models of NF and NP with the variation of the stiffness and density.
- table S3. Numerical values of the membrane.
- table S4. Langmuir and Freundlich isotherm parameters of dye adsorption on SNF/HAP nanocomposites.
- table S5. Langmuir and Freundlich isotherm parameters of metal ion adsorption on SNF/HAP nanocomposites.
- table S6. Kinetic parameters of second-order adsorption kinetic models for metal ions on SNF/HAP nanocomposites.
- table S7. Estimated total cost for preparing 1 g of nanoadsorbents.
- table S8. Maximum sorption capacities of metal ions with different nanomaterials.
- References (*54–101*)

Other Supplementary Material for this manuscript includes the following:
(available at advances.sciencemag.org/cgi/content/full/3/4/e1601939/DC1)

- movie S1 (.mov format). Movie of MD simulation of the SNF/HAP assembly process during deposition, with surface energy γ set as 0 J/m^2.
- movie S2 (.mov format). Movie of MD simulation of the SNF/HAP assembly process during deposition, with surface energy γ set as 0.217 J/m^2.
- movie S3 (.mov format). Movie of MD simulation of the SNF/HAP assembly process during deposition, with surface energy γ set as 0.53 J/m^2.
- movie S4 (.mov format). Movie of preparation of SNF/HAP syringe ultrafilters.
- movie S5 (.mov format). Movie showing that top-down prepared SNF dispersions are directly passing through the 5-µm syringe macrofilter.

Supplementary Materials

Supplementary movies:

movie S1. Movie of MD simulation of the SNF/HAP assembly process during deposition, with surface energy γ set as 0 J/m^2.

Description: Coarse-grained computational MD simulation for SNF/HAP assembly and deposition. The blue and red beads are SNF and HAP, respectively. In this case (weak interaction between SNF and HAP, surface energy γ set as 0 J/m^2), SNFs are assembled into a continuous network during the deposition process and their deposition rate is smaller than that of HAP flakes that lack such self-assembly process. The details can be found in Section 6.

movie S2. Movie of MD simulation of the SNF/HAP assembly process during deposition, with surface energy γ set as 0.217 J/m^2.

Description: Coarse-grained computational MD simulation for SNF/HAP assembly and deposition under intermediate SNF/HAP interaction (surface energy γ set as 0.217 J/m^2). The blue and red beads are SNF and HAP, respectively. The details can be found in Section 6.

movie S3. Movie of MD simulation of the SNF/HAP assembly process during deposition, with surface energy γ set as 0.53 J/m^2.

Description: Coarse-grained computational MD simulation for SNF/HAP assembly and deposition. The blue and red beads are SNF and HAP, respectively. In this case (strong interaction between SNF and HAP, surface energy γ set as 0.53 J/m^2), SNFs and HAP flakes are well mixed by self-assembly before being deposited on the substrate. The details can be found in Section 6.

movie S4. Movie of preparation of SNF/HAP syringe ultrafilters.

Description: The SNF/HAP multilayer membranes can be directly formed on a commercial syringe filter (pore size: 5 μm) by hand-operated extrusion. The first step, we show that water in SNF/HAP dispersion can be removed by hand-operated extrusion. In this process, the SNF/HAP composites can stand on syringe macrofilter substrates and form multilayer nanoporous structures. Then, in the second step, we show that this fresh-made SNF/HAP syringe ultrafilter can be directly used to filter 185 µM Alcian Blue 8GX solution.

movie S5. Movie showing that top-down prepared SNF dispersions are directly passing through the 5-µm syringe macrofilter.

Description: This movie is a control experiment. As shown in Movie 4, 0.2 wt% SNF/HAP dispersion can form syringe ultrafilter by hand-operated extrusion, but top-down prepared SNF dispersion (0.2 wt%) directly passes through the 5 µm syringe filter under the same process.

section S1. Experimental section.

Materials. Sodium bicarbonate, $NaHCO_3$ (ACS reagent, ≥99.7%, Sigma-Aldrich, USA); L-tryptophan(Sigma-Aldrich, USA); Calcium chloride, $CaCl_2$ (anhydrous, granular, ≤7.0 mm, ≥ 93.0%, Sigma-Aldrich, USA); Disodium hydrogen phosphate, Na_2HPO_4 (Sigma-Aldrich, USA); Green fluorescent protein (recombinant protein, synthesis in lab); Cytochrome c (Cytochrome c from equine heart, Sigma-Aldrich, USA); Bovine serum albumin (lyophilized powder, ≥ 95%, Sigma-Aldrich, USA); Gold nanoparticles (5 nm diameter, OD 1, stabilized suspension in citrate buffer, Sigma-Aldrich, USA); Alcian Blue 8GX (powder, Sigma-Aldrich, USA); Brilliant Blue G (pure powder, Sigma-Aldrich, USA); Orange G (dye content ≥ 60%, Sigma-Aldrich, USA); Eosin B (certified by the biological stain commission, dye content 90%, Sigma-Aldrich, USA); Brilliant blue R-250 (for microscopy, Sigma-Aldrich, USA); Alizarin Red S (Sigma-Aldrich, USA); Direct Red 81 (dye content 50%, Sigma-Aldrich, USA); Fluorescent Brightener 28 (Sigma-Aldrich, USA); Rhodamine B (powder, ≥ 95%, Sigma-Aldrich, USA); Congo Red (dye content ≥ 85%, Sigma-Aldrich, USA). Graphene oxide (4 mg/mL dispersion in H_2O, Sigma-Aldrich, USA)

Characterization: Atomic force microscopy (AFM) images of SNFs were performed using an Asylum Research MFP-3D-Bio Atomic Force Microscopy (Asylum Research, an Oxford Instruments Company, Santa Barbara, CA). Igor Pro 6.36 (WaveMetrics, Inc., Lake Oswego, OR) image analysis software was used to determine the heights of observed structures. Scanning electron microscopy (SEM) images of SNF, HAP and SNF/HAP membranes and energy-dispersive X-ray spectroscopy (EDX) mapping of SNF/HAP membranes were characterized by Ultra 55 field emission scanning electron microscope SEM coupled with an EDAX EDX system (Carl Zeiss AG, Oberkochen, Germany) at an acceleration voltage of 5 kV. To prevent electrical charging, all the specimens were deposited with a 5-nm-thick Pd/Pt layer before observation. The X-ray diffraction (XRD) spectrum of HAP crystal was obtained using a Bruker D8 Discover diffractometer with the 2D detector of GADDS (Bruker, Karlsruhe, Germany. The experiment was performed at MIT Center for Materials Science and Engineering). The experiments were performed using Cu Kα radiation (λ=1.54 Å) at 40 kV and 20 mA. The Fourier transform infrared spectroscopy (FTIR) spectrum of SNF/HAP membranes was collected by using Jasco FTIR-6200 spectrometer (Jasco Instruments, Easton, MD). For each measurement, 64 interferograms were co-added and Fourier-transformed employed a Genzel-Happ apodization function to yield spectra with a nominal resolution of 4 cm^{-1}. The AFM and SEM experiments were performed at the Harvard University Center for Nanoscale Systems (CNS), a member of the National Nanotechnology Coordinated Infrastructure Network (NNCI), which is supported by the National Science Foundation under NSF award no. 1541959.

Modeling of adsorption kinetics, isotherms: In order to evaluate the adsorption kinetic and mechanism of SNF/HAP composites for dyes and metal ions, the pseudo-second (PS) order models have been exploited to analyze the experimental data. The pseudo-second order equation based on adsorption equilibrium capacity assumes that the rate of occupation of desorption sites is proportional to the square of the number of unoccupied sites (*54*). A linear form of pseudo second-order kinetic model (*54*) is express by eq.

$$\frac{\mathrm{t}}{q} = \frac{1}{k_2 q_e^2} + \frac{t}{q_e} \tag{1}$$

where k_2 is the rate constant (g mg^{-1} min^{-1}) of pseudo second-order kinetic model for adsorption, and q_e is the adsorption capacity calculated by the pseudo-second order model (mg g^{-1}).

To investigate the efficacy of adsorption, Langmuir and Freundlich models were used to fit experimental data. The Langmuir model assumes that a monomolecular layer is formed when adsorption takes place without any interaction between adsorbed molecules (*55*). The form of the Langmuir isotherm (*55*) can be represented by the following equation

$$q_e = q_m \frac{K_L C}{1+K_L C} \tag{2}$$

where q_e is the amount of metal ions adsorbed per gram of adsorbent (mg g^{-1}), C denotes the equilibrium concentration of metal ions in solution (mg L^{-1}); k_L represents the Langmuir constant (L mg^{-1}) that relates to the affinity of binding sites and q_m is a theoretical limit of adsorption capacity when the monolayer surface is fully covered with metal ions to assist in comparison of adsorption performance (mg g^{-1}). The Freundlich model assumes a heterogeneous adsorption surface and active sites with different energy (*56*). The Freundlich model is given as

$$q_e = K_F C^{1/n} \tag{3}$$

where q_e is the amount of metal ions adsorbed per gram of adsorbent (mg g^{-1}); C is the equilibrium metal ion concentration in solution (mg L^{-1}); K_F and n are the Freundlich constants, which represent the adsorption capacity and the adsorption strength, respectively. The magnitude of $1/n$ quantifies the favorability of adsorption and the degree of heterogeneity of the adsorbent surface.

The amount of adsorbed metal ions on the adsorbents (q, mg g^{-1}) was calculated as follows

$$q_t = (C_0 - C_t) \times \frac{V}{m} \tag{4}$$

where C_0 and C_t are the metal ion concentrations (mg L^{-1}) at the beginning of the experiment and after a period of time t; V is the initial volume of the solution (L); and m is the adsorbent weight (g).

section S2. Coarse-grained computational model for SNF/HAP assembly and deposition.

Elastic network models were built in mechanics and geometry feature of the unit building blocks. Each SNF flake and HAP thread are modeled by an elastic network with carefully chosen elastic constants to match the materials' elastic properties and mass concentrated at the junction beads to match the material densities, such a strategy has been proven to be efficient to model other biological materials (*53*). A SNF fiber was modeled by a series of mass beads connected by a series of harmonic springs and a HAP flake was modeled by mass beads connected by a rectangular spring network (**fig. S1**). For SNF the total energy function was given by

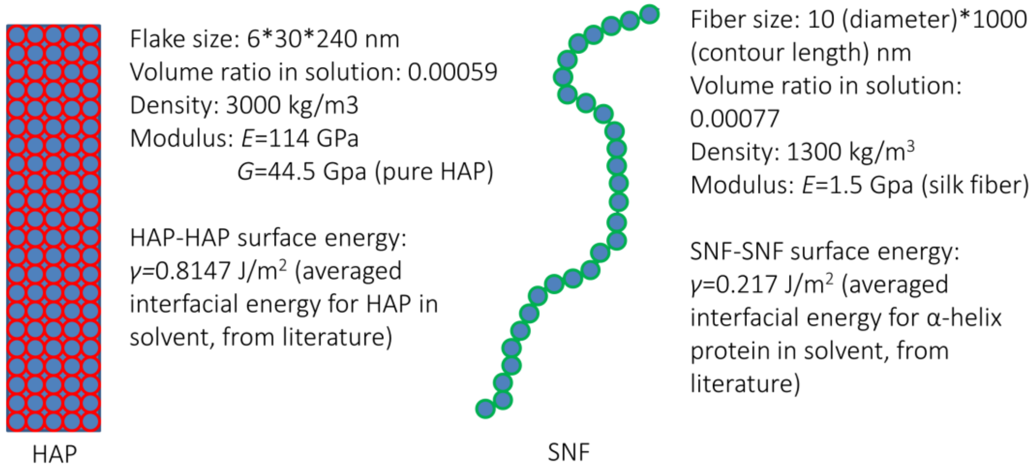

fig. S1. Schematic figure of the coarse-grained computational model for HAP and SNF.

$$E = E_T + E_B + E_{non-bond} \tag{5}$$

Where E_T is the tensile deformation energy for fiber stretching, E_B for bending and $E_{non-bond}$ for non-bonded interaction with other SNF beads and HAP beads. Each energy term was defined by

$$E_T = \sum \varphi_T(r), \quad \varphi_T(r) = k(r - r_0)^2 \tag{6}$$

$$k = E_{SNF}A/(2r_0) = E_{SNF}\pi d^2/(8r_0) \tag{7}$$

Where d is the silk fiber diameter, r_0 is the equilibrium distance between two neighbouring beads, $E_{SNF} = 1.5$ GPa is the average secant modulus of silkworm silk under tensile loading. The bending energy was given by

$$E_B = \sum \varphi_B(\theta), \varphi_B(\theta) = K_B(\theta - \theta_0)^2 \tag{8}$$

$$K_B = \frac{E_{SNF}I_t}{2r_0} = \frac{E_{SNF}\pi d^4}{128r_0} \tag{9}$$

The mass of the bead is given by

$$m_{SNF} = \pi d^2 r_0 \rho / 4 \tag{10}$$

where ρ =1300 kg/m^3 is the density of silk fiber.

For HAP, each bond stiffness is given by

$$k = E_{HAP} t^2/(2t) = E_{HAP} t/2 \tag{11}$$

Where $E_{HAP} = 114$ GPa is Young's modulus of HAP and t=6 nm is the average thickness of HAP flakes. For angular spring that connect two neighboring bond with 180° angle, its stiffness was defined by the bending stiffness of the HAP flake

$$K_{B1} = \frac{E_{HAP} I_t}{2r_0} = \frac{E_{HAP} t^3}{24} \tag{12}$$

For angular spring that connects two neighboring bonds with 90° angle, its stiffness was defined by the shear stiffness of the HAP flake

$$K_{B2} = \frac{1}{8} G_{HAP} t^3 \tag{13}$$

The mass of HAP bead was given by

$$m = \ t^3 \rho \tag{14}$$

Where ρ =3×10^3 kg/m^3 is the density of HAP. For interfacial interactions between two molecules

$$E_{non-bond} = \sum \varphi_{non-bond}(r), \tag{15}$$

$$\varphi_{non-bond}(r) = 4\epsilon \left[(\frac{\sigma}{r})^{12} - (\frac{\sigma}{r})^{6} \right] \tag{16}$$

For interaction between a pair of non-bonded SNF-SNF beads $\epsilon_{SNF-SNF} = \gamma_{NF-SNF} d r_0$, γ=0.217 J/m^2 (protein adhesion energy), from literature (*57*), $\sigma = 2^{\ -1/6} d$

For interaction between a pair of non-bonded HAP-HAP beads $\epsilon_{HAP-HAP} = \gamma t^2$, γ=1.180 (Cleavage energy)- 0.3653(Water immersion energy)=0.8147 J/m^2 , from literature (*58*), $\sigma = 2^{-1/6}t$

For interaction between a pair of non-bonded SNF-HAP beads $\epsilon = \gamma_{HAP-SNF} d r_0$, $\sigma = 2^{-1/6}d$

HAP-SNF surface energy $\gamma_{HAP-SNF}$ was not certain as it depended on the molecular structure and the hierarchy structure of the interface in contact. The effect of its numerical value was discussed in the main text and it was found that effects important for forming the layered structure.

The initial geometry of the simulation box was generated by our Matlab script. The box size was 0.5*0.5*50 µm^3 with 50 µm along the axis of the flow direction and periodic boundary conditions were applied to the other two directions. A collection of SNFs were generated to have a length distribution with a mean value of 1 µm and standard deviation of 0.4 µm. HAPs were generated to have a uniform size as 6*30*240 nm^3. The ratio of numbers of SNF and HAP molecules were computed according to their volume ratio in solution as the experiments. The volume ratio of both HAP and SNF were increased by 16 times to account for the effect of getting concentrated at the bottom of the bottle and overcame the limitation of size and time of simulations. Each SNF and HAP was initially randomly placed and oriented in the simulation box as shown in **fig. S2a**. A substrate modeled by LJ9-3 potential at the bottom of the simulation box (*z*=0) was used to simulate the substrate that supports the SNF-HAP deposition. The initial geometry of the simulation box is presented in **fig. S2a**.

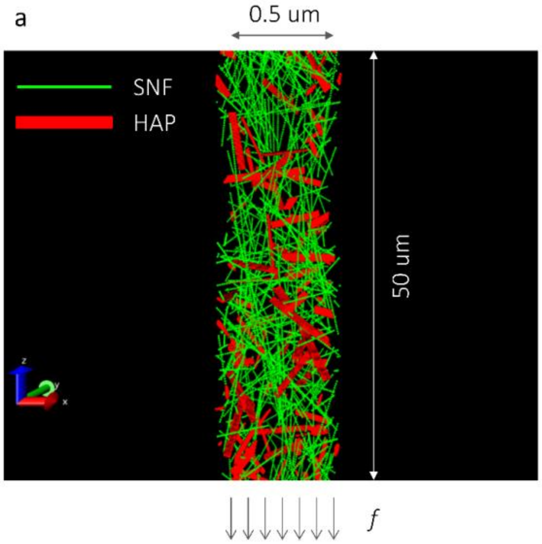

Subjected to a gravity field that accounts for the drag force from the water flow

b

$f_{drag} = -6\pi\mu R v$

The bead radius is given by $R_{silk} = (\frac{3}{4} * (d^2 r_0/4))^{1/3}$= 5.72 nm, $R_{Hap} = (\frac{3}{4\pi} * t^3)^{1/3}$= 3.72 nm, for $v = 250\ \mathrm{m/s}$

$f_{drag\_silk} = -6\pi\mu R v$ =333.8 kcal/mol/A
$f_{drag\_hap} = -6\pi\mu R v = 217.1$ kcal/mol/A

$a_{drag\_silk} = 0.00055$ kcal/mol/A/amu
$a_{drag\_hap} = 0.00085$ kcal/mol/A/amu

fig. S2. Simulation setups and related parameters for SNF/HAP assembly and deposition modeling. The simulation setups (**a**) and related parameters (**b**) for SNF/HAP assembly and deposition modeling.

table S1. Numerical values of the physical parameters of the coarse-grained model.

Parameter and units	**Numerical value for SNF**	**Numerical value for HAP**
Equilibrium bead distance r_0, t (in nm)	10	6
Molecule geometry in other dimensions d (in nm)	10	30×240
Tensile stiffness parameters k (in kcal/mol/A^2)	8.50	492
Equilibrium angle θ_0 (in rad)	π	π, $\pi/2$
Bending stiffness parameter K_B (in kcal/mol)	5300	1.5×10^5, 1.73×10^5
SNF-SNF bead non-bonded interaction energy (in kcal/mol)	3125	
SNF-SNF bead non-bonded interaction equilibrium distance (in nm)	8.9	
HAP-HAP bead non-bonded interaction energy (in kcal/mol)	4223	
HAP-HAP bead non-bonded interaction equilibrium distance (in nm)	5.3	
SNF-HAP bead non-bonded interaction energy (in kcal/mol)	$\boldsymbol{\gamma_{HAP-SNF} d r_0}$	
SNF-HAP bead non-bonded interaction equilibrium distance (in nm)	8.9	
Mass of each mesoscale particle m (in amu)	614650	390100
Drag force factor $\frac{f_{drag}}{m}$ (in kcal/mol/A/amu)	0.00055	0.00085

We implicitly model the water flow by applying the drag force on all the coarse-grained beads. The simulation setups and related parameters are summarized in **fig. S2b**. HAP and SNF beads were subjected to a gravity field that accounts for the drag force from the water flow. The drag force was given by the Stokes' law as

$$f_{drag} = -6\pi\mu R v \tag{17}$$

Where the effective bead radius is given by $R_{silk} = (\frac{3}{4} * (d^2 r_0/4))^{1/3} = 5.72$ nm, $R_{Hap} = (\frac{3}{4\pi} * t^3)^{1/3} = 3.72$ nm, $\mu = 8.6 \times 10^{-4}$ Pa · s is the fluid viscosity constant of water at room temperature and *v*=250 m/s is the flow velocity we used in our simulations and its large numerical value is used to overcome the limitation of simulation time scale. All the numerical values of the physical parameters of the model are summarized in **table S1.**

We varied the numerical value of $\gamma_{HAP-SNF}$ from 0 to 0.53 J/m^2 in our simulations and found this interfacial energy highly affected the geometry of the multilayer membrane as it deposited on the substrate, which was shown in the main text. The distributions of the mass ratio between HAP and SNF as functions of the coordinate along the membrane thickness direction for the 3 membranes are summarized in **fig. S3**. For a weak HAP/SNF interaction, the transition from more HAP to more SNF region took place closer to the middle of the membrane. In opposite, for a strong HAP/SNF interaction, the transition from more HAP to more SNF region took place closer to the top surface, as the two materials were more homogeneous mixed before forming the membrane.

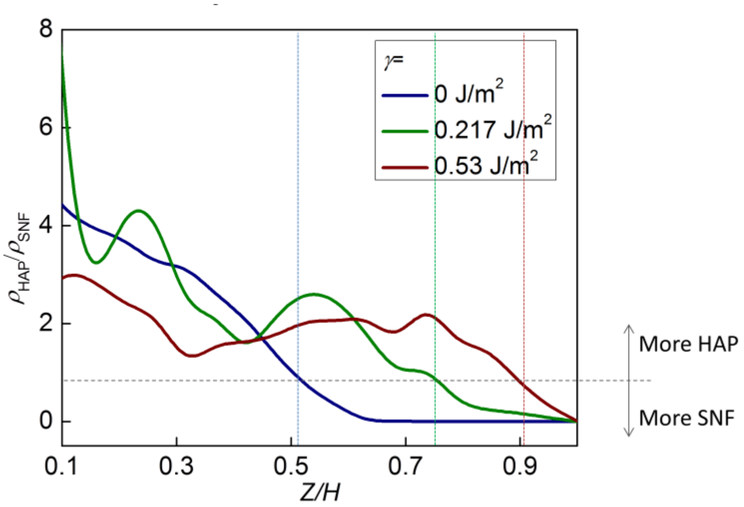

fig. S3. Distributions of the mass ratio between HAP and SNF as functions of the coordinate along the membrane thickness direction for the three membranes assembled with different γ values. The dash line suggests the transition from more HAP to more SNF region, for which the stronger HAP/SNF interaction leads to a more homogenously mixed material.

Many simulations were run to account for the variation of the stiffness and density for the broad range of protein nanofibers (NFs) and calcium based minerals nanoplates (NPs). A wide range of mineral densities (from 1×10^3 to 3×10^3 kg/m^3) and stiffnesses of NFs (from 0.3 to 15 GPa) and NPs (from 114 to 570 GPa) were found for the physical properties of these models (table S1.1). The membrane deposition process was repeated for these 5 different models by applying $\gamma_{HAP-SNF}$=0, 0.217 and 0.53 J/m^2 (15 individual extra simulations) and a summary of the distributions of the mass ratio between HP and NF as a function of the coordinate along the membrane thickness direction for the 15 membranes (**fig. S4)**. The $\gamma_{HAP-SNF}$ consistently played the predominant role to govern the membrane assembly, as $\gamma_{HAP-SNF} < 0.217$ always led to a multilayer structure as the mass ratio between NP and NF exponentially decays from a high value to 0 as away from the substrate. However, for high $\gamma_{HAP-SNF}$ NPs and NFs were well mixed to form a more homogeneous hybrid membrane material.

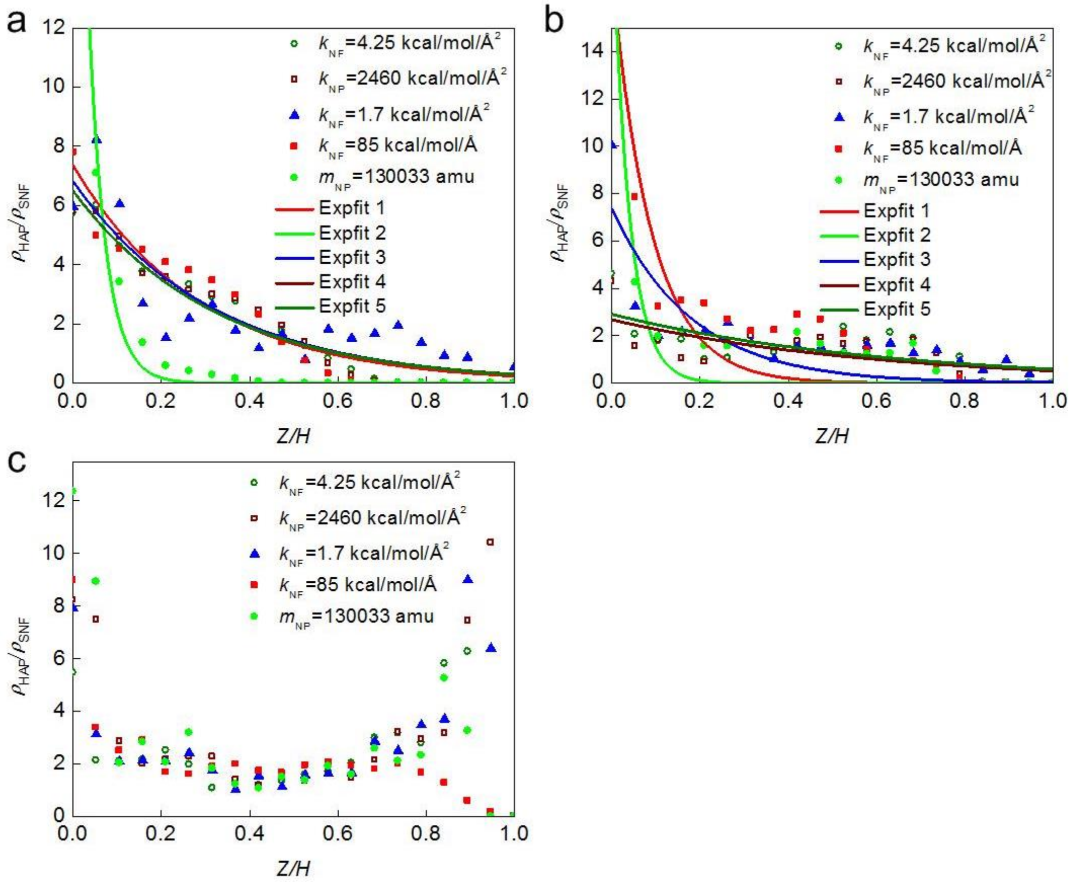

fig. S4. Distributions of the mass ratio between NP and NF as functions of the coordinate along the membrane thickness direction for the 15 membranes assembled with different γ values. The distributions of the mass ratio between NP and NF as functions of the coordinate along the membrane thickness direction for the 15 membranes assembled with different $\gamma_{HAP-SNF}$ values ($\gamma_{HAP-SNF}$=0, 0.217 and 0.53 J/m^2 for panel **a**, **b** and **c**, respectively). The exponential fitted curves in panel **a** and **b** suggest that the mass ratio decays from a high value to 0 as away from the substrate, agreeing with the simulation results of a multilayer structures.

table S2. Numerical values of the physical parameters of the five coarse-grained models of NF and NP with the variation of the stiffness and density.

Model #	E_{NF} **(GPa)**	E_{NP}**(GPa)**	ρ_{NF} **(kg/m^3)**	ρ_{NP}**(kg/m^3)**
1	**0.75**	114	1300	3000
2	1.5	**570**	1300	3000
3	**0.3**	114	1300	3000
4	**15**	114	1300	3000
5	1.5	114	1300	**1000**

section S3. The self-assembly process and structure of SNFs.

In a typical process, aqueous silk fibroin (~0.1 wt%) solution was assembled into elongated SNFs at 60 °C and incubated for 1 week without requirements of other processes. The resulting solution was transparent (**fig. S5a**), with strong birefringent under polarized light (**fig. 5a**), indicating the presence of a nematic phase of SNFs (*37*,*59*). The structural features of the SNFs were determined by atomic force microscopy (AFM); the SNFs exhibited a necklace-like morphology, with a height of 3-4 nm and a contour length up to 5 µm (**fig. 2a and S5b,c**).

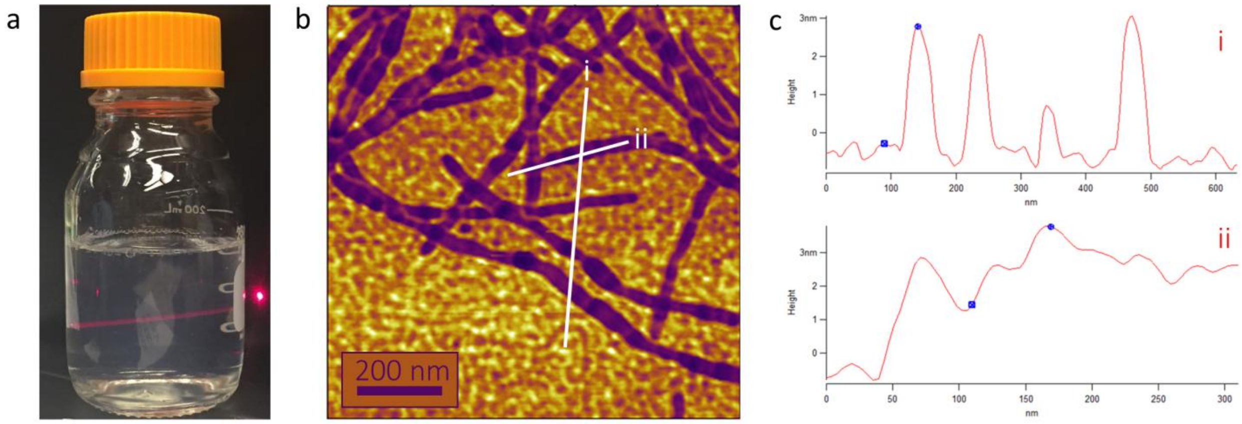

fig. S5. Visual appearance and AFM image of SNFs. (**a**) Photograph of silk nanofibril (SNF) solution (~0.1 wt%). (**b**) AFM phase image of SNFs. (**c**) Height profile collected along the indicated colored lines. Careful examination of the image b and height profile (ii) reveals that the SF nanofibrils have a necklace-like morphology. The center-to-center distance of the beads is ~25 nm.

section S4. Synthesis of HAP nanocrystals via biomineralization approach.

The biomineralization was carried out in 0.1 wt% aqueous SNF solution. The biomineralized HAP was confirmed by X-ray diffraction (XRD) and Fourier transform infrared spectroscopy (FTIR) characterization (**fig. S6**). The XRD profile of biomineralized HAP showed same peaks with standard diffraction peaks of HAP crystal (**fig. S6a**). In FTIR spectra (**fig. S6b**), two bands in the 1700-1500 cm^{-1} range are amide I and amide II of SNFs. The secondary structures of SNF were disclosed via assessment of the amide I bands (1700–1600 cm^{-1}). The spectra in the amide I bands showed a similar shape to degummed silk fibers (*60*); a sharp peak at 1620 m^{-1} and a shoulder at 1695 cm^{-1}, which were assigned to β-sheets and β-turns of the hairpin-folded antiparallel β-sheet structure (*60*), respectively. These results indicated that the SNFs were mainly composed of β-sheet. The 1200–900 cm^{-1} region with the peak at 1037 cm^{-1} was assigned to PO_4 bending vibration of HAP crystal.

The morphology of SNF-biomineralized HAP was disclosed by scanning electron microscopy (SEM), it can be found all HAP nanocrystals had similar shape and size and no aggregates were observed (**fig. S7**), in contrast to the flower-like HAP aggregates in silk solution from control experiments (**fig. S8**) as well as found in most reports (*61*-*63*).

To understand the dispersed state of SNF and HAP in solution, the SNF/HAP solution was frozen with liquid nitrogen, followed by freeze drying. SEM images of the resulting powders revealed that SNFs formed uniformly connected networks (**fig. S9a**) and that the synthetic HAP nanocrystals were held and stabilized by the porous SNF networks (**fig. S9b**).

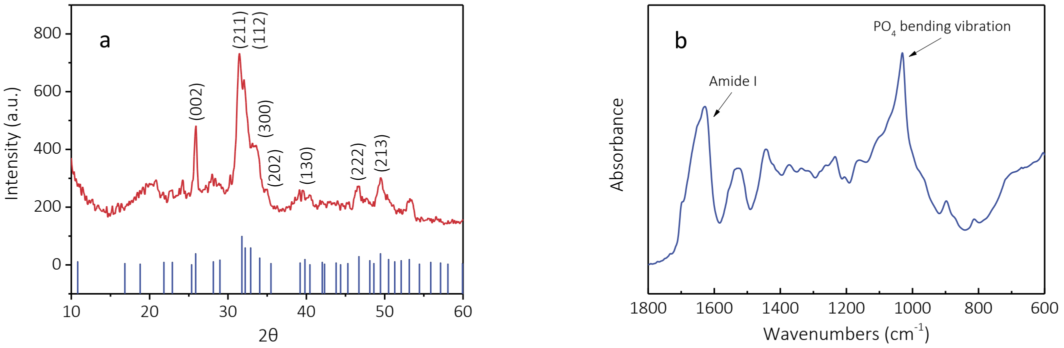

fig. S6. XRD profile and Fourier transform infrared spectrum of biomineralized HAP nanocrystals. (**a**) XRD profile of biomineralized hydroxylapatite (HAP) nanocrystals. The expected standard diffraction peaks according to the Joint Committee on Powder Diffraction Standards (JCPDS) for HAP are shown as discrete bars (JCPDS No. 09–0432). (**b**) FTIR spectrum of SNF/HAP membrane.

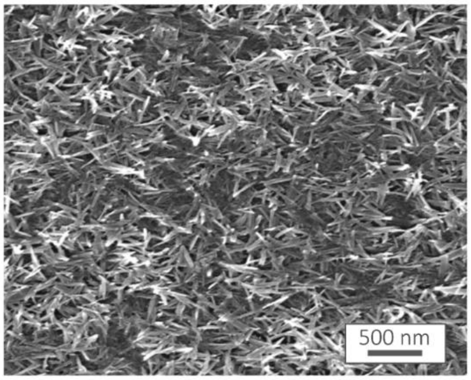

fig. S7. SEM image of biomineralized HAP nanocrystals.

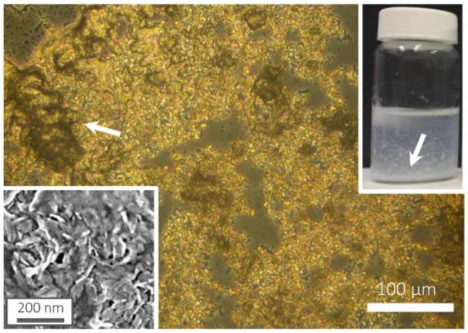

fig. S8. SF solution induced the growth of HAP at 37°C for 1 week. The largest (central) image is the optical microscopy image of biomineralized HAP. The white arrow indicated the large aggregates of HAP crystals. The left bottom picture is a SEM image of HAP flower-like aggregates. The right top image is a photograph of silk fibroin solution after biomineralization of HAP. The white arrow shows that the HAP aggregates were precipitated to the bottom of the bottle.

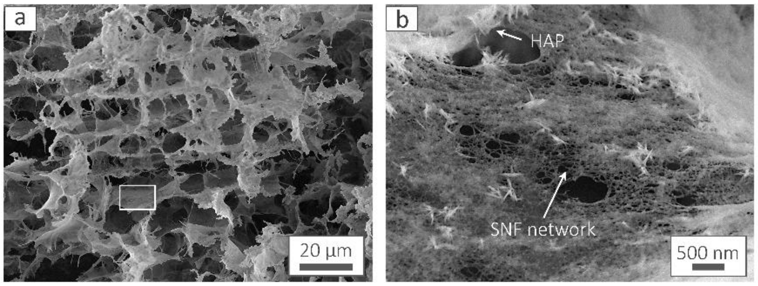

fig. S9. Mesostructure of SNF/HAP solution after liquid nitrogen freezing and freeze-drying. Picture (**b**) is a partial enlarged image of picture (**a**). These two images revealed that SNFs formed a continuous mesh structure and the HAP nanocrystals stood on the SNF mesh.

section S5. Multilayer membrane formation and their properties.

The membranes were formed by vacuum filtration. Typically, 3 mL of SNF/HAP dispersion generated a membrane that was approximately 4 μm thick using a filtration mold that was 3.5 cm in diameter (all of the membranes in this paper were prepared using the same mold), and the volume of the dispersion (with a concentration of ~0.2 wt%) was linearly correlated to membrane thickness (**fig. S10**).

The SNF/HAP membranes with a thickness larger than 4 μm could be easily moved from the substrate and even could undergo cutting, bending and twisting without damage (fig. S11a-c). Moreover, the membranes were stable in water without dissolution for more than one month (fig. S11d). This property ensured the durability of membranes during the standby and purification processes. Tensile tests were carried out to measure the mechanical properties of the materials (**fig. S12**). The mechanical data were recorded by Instron tensile machine. All of the tests were carried out at ~25 °C and 50% relative humidity with a tensile speed of 1 mm min^{-1}.

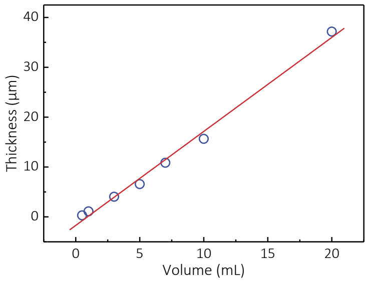

fig. S10. Linear relationship between the volume of SNF/HAP solution and the resultant membrane thickness.

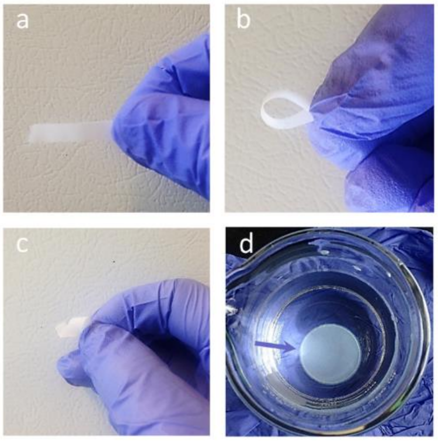

fig. S11. Images of SNF/HAP membranes after moving from the substrate with a thickness of 4 μm. (**a-c**) The membrane after cutting (a), during bending (b) and twisting (c). (**d**) The membrane was immersed in water for 1 month at room temperature.

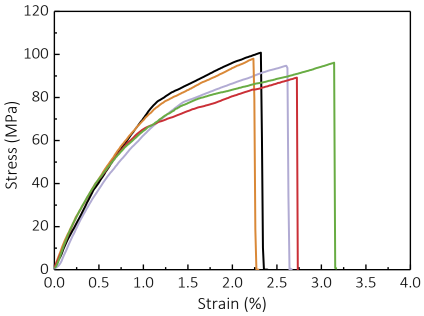

fig. S12. Stress-strain curves of as-cast SNF/HAP membrane with a thickness of 37 μm.

section S6. Multilayer structure of SNF/HAP membrane.

The SNF/HAP membranes had highly ordered multilayer structures and showed nacre-like brick-and-mortar structure (fig. S13). The numbers of the layers increased with more volume of SNF/HAP solution to prepare the membranes (fig. S14). All of the membranes showed a brick-and-mortar-like structure with alternating SNF and HAP layers (fig. S14), suggesting by both geometric feature and heterogeneous element distributions (fig. S15).

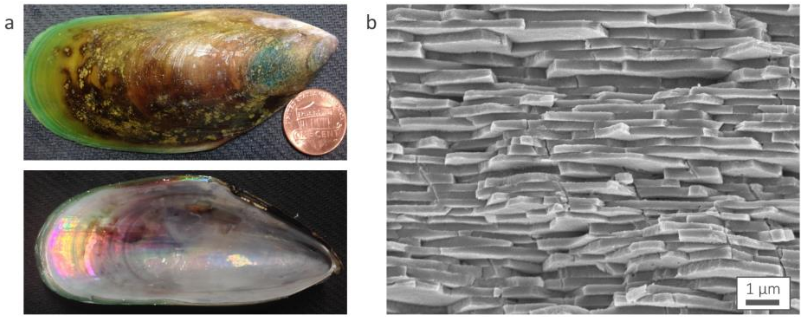

fig. S13. Multilayer structure of nacre. (**a**) The photographs of a mussel shell. (**b**) Cross-sectional SEM image of a mussel shell. The clear multilayer brick-and-mortar structure can be found, the thickness of each layer is about 200-400 nm.

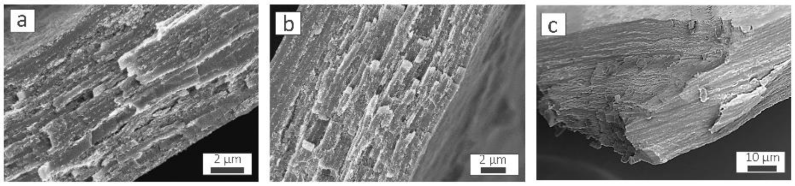

fig. S14. SEM images of SNF/HAP membranes. SEM images of SNF/HAP membranes prepared from (**a**) 7 mL, (**b**) 10 mL and (**c**) 20 mL SNF/HAP dispersion (~0.2 wt%) using a filtration mold with inner diameter of 3.5 cm.

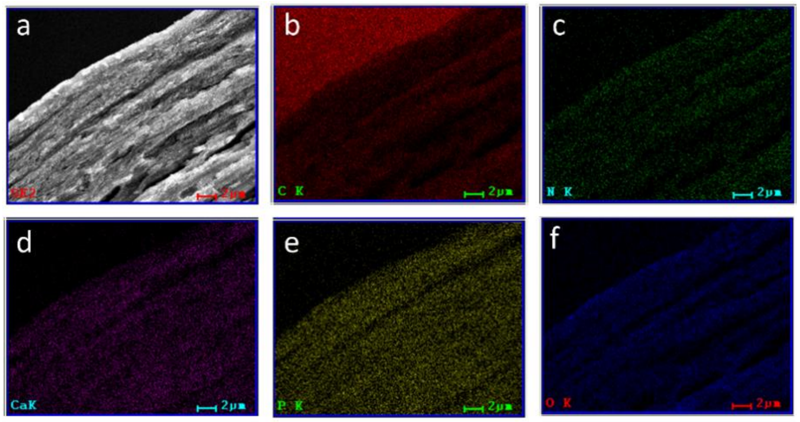

fig. S15. Elemental analysis of the cross-sectional SNF/HAP membranes. Elemental maps are shown for carbon (picture b), nitrogen (picture c), calcium (picture d) phosphorus (picture e), and oxygen (picture f).

section S7. Multitypes of SNF/HAP multilayer membranes.

The SNF/HAP multilayer membranes could be formed through different facile processing methods, such as cylinder extrusion (fig. S16a, Movie 4) and vacuum filtration (fig. S16b,c). SNF/HAP composites could even stand on the substrate with porous size much (more than 100 times) larger than the size of SNF and HAP (fig. S16c). As controls, other nanomaterials, such as top-down SNF (*11*,*64*) (**Movie 5**) and graphene oxide (**fig. S16d**), directly passed through the filter. The top-down SNF dispersion was prepared according to our previous reports (*11*,*64*). Briefly, the degummed *Bombyx mori* silk fibers were immersed in hexafluoroisopropanol (HFIP) solution with a weight ratio of 1:30 and were mixed by vortexing. Then the sealed silk fiber/HFIP mixture was incubated at 60 °C to partially dissolve the silk fibers to silk microfibrils

(SMFs). After 24 hours, the resultant SMF pulp blend was dried to evaporate the HFIP. After totally drying, the SMFs were placed in water with a weight ratio of 1:200 with continuous stirring or shaking, followed by removal of undissolved silk. Finally, the SMFs/water mixture was sonicated at 120 µm amplitude and 20 KHz frequency, at intervals of 10 sec. After 1h, the exfoliated SNFs dispersion was harvested by centrifugation at 10,000 rpm for 20 min. The graphene oxide aqueous dispersion (1 mg/mL) was purchased from Sigma-Aldrich, USA.

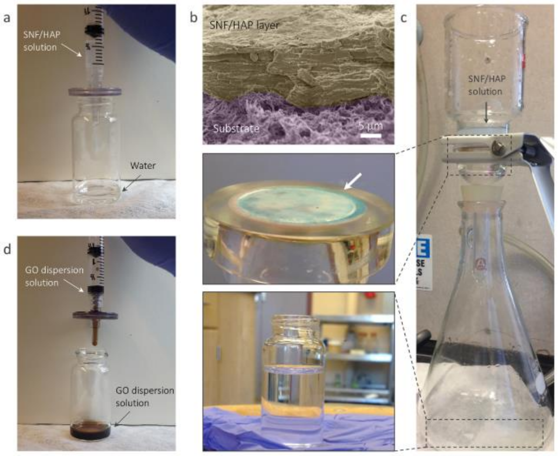

fig. S16. Multitypes of SNF/HAP multilayer membranes. (**a**) Photograph of SNF/HAP on a 5 µm thick PVDF microfilter membrane, water easily passes through. (**b**) SEM image of SNF/HAP membrane on a 5 µm thick PVDF microfilter membrane formed through syringe extrusion. Pseudo-color applied to distinguish the SNF/HAP and syringe filter membranes. The cross-section of the SNF/HAP membrane indicates that the brick-and-mortar-like structure even formed during simple hand-extrusion. (**c**) Photographs of SNF/HAP membranes formed on a straight-wall, glass funnel with a pore size of 40-50 µm after filtration of 20 mL ~0.2 wt% SNF/HAP solution. The solution in the bottle is penetrant and transparent, indicating that the SNF/HAP composite was completely held by glass funnel during filtration processing. (d) The photograph to show that graphene oxide (1 mg/mL) freely passed through a syringe filter with a pore size of 5 µm. The size of graphene oxide (~2 µm width) was smaller than the pore size of syringe filter, and graphene oxide nanosheets do not form a continuous network structure.

section S8. Mechanical model of SNF/HAP membrane for water filtration.

The filtration model was built as schematically shown (**fig. S17**). The membrane was composed of alternative SNF with thickness h_1 and HAP with thickness h_2. The radius of the pores was r_1 (SNF) and r_2 (HAP). The density of pores in the plane was α_1 (SNF) and α_2 (HAP). The total thickness of the membrane was H.

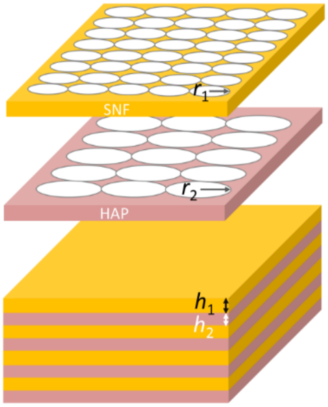

fig. S17. Schematic of SNF/HAP multilayer filtration membrane.

The Reynolds number of flow in the pores was computed via $Re = \frac{\rho v D}{\mu}$, where ρ=1×10^3 kg·m^{-3} and μ=0.001 kg·m^{-1}·s^{-1} was the density and viscosity of water obtained at room temperature, respectively. For filtration with the current membrane, the velocity $v < 1$ m·s^{-1} and pore diameter D<30 nm applied to all the study cases and thus Re<0.03 was obtained, which was in the laminar flow region. Hence the Hagen–Poiseuille equation was applicable and the pressure drop for a single pore in the SNF layer is given by

$$\Delta P_{\mathrm{SNF}} = \frac{8 k_1 \mu h_1 Q_1}{\pi r_1^4} \tag{18}$$

Where Q_1 is the volume rate through a pore and k_1 accounts for the pore shape. The total volume rate is $Q = \alpha_1 Q_1 A$, where A is the total cross-section area of the membrane for filtration. Similarly, the pressure drop for a single pore in the HAP layer was given by

$$\Delta P_{\mathrm{HAP}}=\frac{8k_2\mu h_2 Q_2}{\pi r_2^4} \tag{19}$$

And the total volume rate kept constant through layers, thereby

$$Q_2 = \alpha_1 Q_1/\alpha_2 \tag{20}$$

The total pressure drop of the entire membrane was given by

$$\Delta P = \sum(\Delta P_{\mathrm{SNF}} + \Delta P_{\mathrm{HAP}}) = \left(\frac{8h_1}{\beta_1 r_1^4} + \frac{8h_2}{\beta_2 r_2^4}\right)\frac{\mu H Q}{A\pi(h_1+h_2)} \tag{21}$$

Where $\beta_1 = \alpha_1/k_1$ and $\beta_2 = \alpha_2/k_2$. The flux of the water flow was therefore given by

$$f_{flux} = \frac{Q}{A\Delta P} = \frac{\pi(h_1+h_2)}{8\mu H\left(\frac{h_1}{\beta_1 r_1^4}+\frac{h_2}{\beta_2 r_2^4}\right)} \tag{22}$$

h_1 and h_2 were fitted by power law according to the experimental measurements, as shown in **fig. S18**.

$$h_1=1405.9H^{-0.15} \tag{23}$$

$$h_2=22072.6H^{-0.54} \tag{24}$$

table S3. Numerical values of the membrane.

Geometric symbol	Experimental measurement value
Thickness of SNF h_1 (nm)	$1405.9H^{-0.15}$
Thickness of HAP h_2 (nm)	$22072.6H^{-0.54}$
Radius of the pores in SNF r_1 ± sd (nm)	4 ± 1
Radius of the pores in HAP r_2 ± sd (nm)	14±2.5

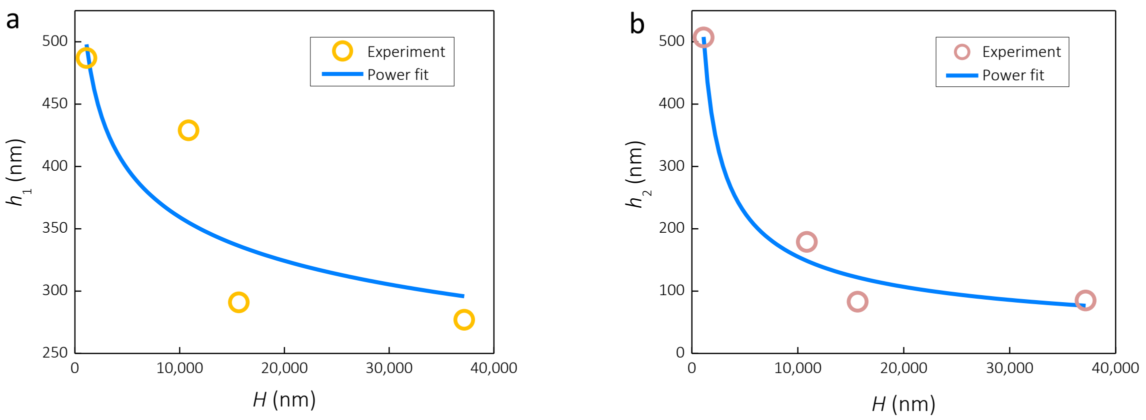

fig. S18. Calculation of SNF and HAP thickness via power-law fittings. Calculation of SNF (**a**) and HAP thickness (**b**) via power law fittings.

Putting (6) and (7) into (5) allowed finding the numerical value of β_1 and β_2 by fitting according to the data points and β_1 $=4\times10^{18}$ m^{-2} and β_2 $=4\times10^{14}$ m^{-2} was found for a good fit with experiments (**fig. S19**). One reason $\beta_1 \gg \beta_2$ is that the $r_1 < r_2$ leads to $\alpha_1 > \alpha_2$. Another reason is that the irregular geometry of the pores in HAP made its drag force much larger than idealized round channel and thus $k_2 \gg k_1$.

For homogeneous membrane with uniform channels, Eq. (18) could be simply reduced to the classical Hagen–Poiseuille equation

$$f_{flux} = \frac{Q}{A\Delta P} = \frac{\pi\beta r^4}{8\mu H} \tag{25}$$

Thus, it was clear that $f_{flux} \sim H^{-1}$ and it was shown that by having the two layers in the SNF-HAP composite help to maintain the flux once the membrane was thicker than the membrane made of pure SNF or HAP. It was noted that β relates to the membrane porosity and pore shape and its numerical value was determined by fitting according to the flux-H relationship. Therefore for pure SNF or HAP membranes their β and r values would be probably very different from those of the SNF or HAP layers within the multilayer assembly. Actually it was the interaction between SNF and HAP made the combination more water permeable, as the pure SNF membrane had much weaker water permeability than the SNF/HAP membrane of the same thickness.

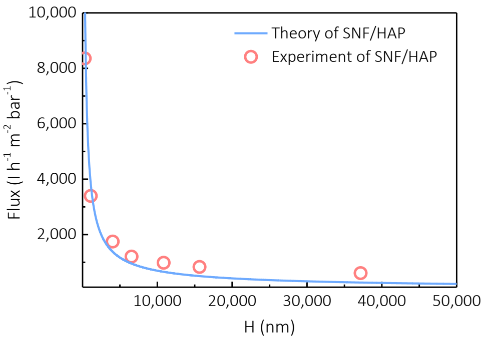

fig. S19. Comparison of theory fluxes of pure SNF, HAP, and SNF/HAP membranes with similar thicknesses. The water volume used in this experiment is 100 mL.

section S9. Dye separation and adsorption performance of SNF/HAP membranes.

Dye separation efficiency is usually unsatisfactory for most ultrathin filtration membranes. However, both the SNF and HAP components in the SNF/HAP membranes have the capability to capture different dyes and are thus suitable for separating dyes from water. We first measured the separation performance of the 4-μm-thick SNF/HAP membranes for 10 mL dye solution through pressure-driven filtration. The membranes exhibited efficient separation for most dyes which are listed in Fig. 4g. The SNF/HAP membranes showed excellent separation performance for 185 μM Alcian Blue 8GX and 398 μM Brilliant Blue G with the rejection of 94±3% and 92±1%, respectively. Since the 4-μm-thick membrane did not show perfect rejection (up to 100%) for most dyes, e.g. 10 mL 601 μM Orange G (rejection: 50±3%), 10 mL 320 μM Eosin B (rejection: 60±2%), 10 mL 17μM Congo Red (rejection: 67±4%) and 5 μM Rhodamine B (84±1%), a 10 mL 5 μM Rhodamine B aqueous solution was selected to study the influence of membrane thickness on separation performance (**fig. S20**). The UV-vis spectra (insert plots in **fig. S20**) with an absorption at 554 nm dropped gradually by increasing membrane thickness from 1 to 37 μm. The calculation demonstrated that rejection reached equilibrium (rejection: 96%) at a membrane with a thickness of 16 μm.

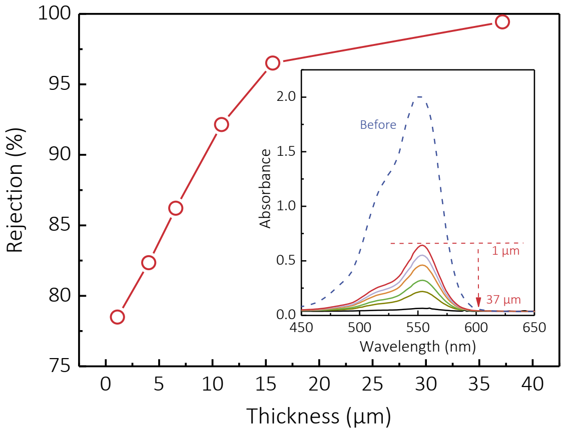

fig. S20. Rejection of 10 ml of 5 μM Rhodamine B aqueous solution with different thicknesses of the SNF/HAP membranes. The insert plot shows UV-vis absorption changes of an aqueous solution of rhodamine B after filtration with SNF/HAP membranes with different thicknesses.

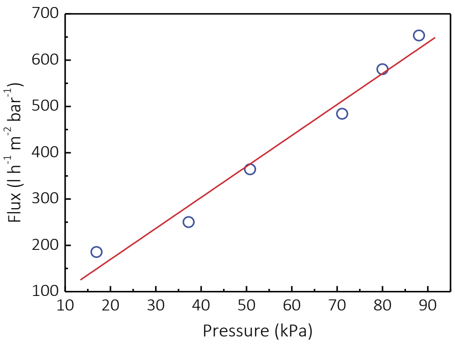

fig. S21. Relationship between pressure and pure water flux of ejection of 37-μm-thick SNF/HAP membrane. The water volume used in this experiment is 10 mL.

The effect of applied pressure on pure water flux and the separation performance of SNF/HAP membranes was estimated by using 37-μm-thick SNF/HAP membranes (**fig. S21**). The linear relationship between pressure and pure water flux can be observed from **fig. S21**. For separation experiments (**fig. S22**), the rejection of Rhodamine B declined continually with increased pressure in the range of 17-88 kPa. This tendency is different from that in more traditional polymer-based membranes since the rejection rate usually increases with pressure because of compression and/or densification of the porous structures. However, as with the new membranes described in the present work, a similar phenomenon was found with graphene- and carbon nanotube-based filtration membranes and was attributed to the enlarged nanochannel pore sizes due to increased pressure (*17*). In addition to this view, the contact/interaction time of dye and membrane components may also play important roles in the pressure response of membranes, in particular, for SNF/HAP membranes. The separation performance of SNF/HAP membranes is not only decided by their pore size but also by their adsorption feature. The adsorption capability of membranes is positively related to contact/interaction time between dyes and membranes, thus this contact time between dyes and membranes will be shortened by increasing the pressure, as a result, that less dye would be removed.

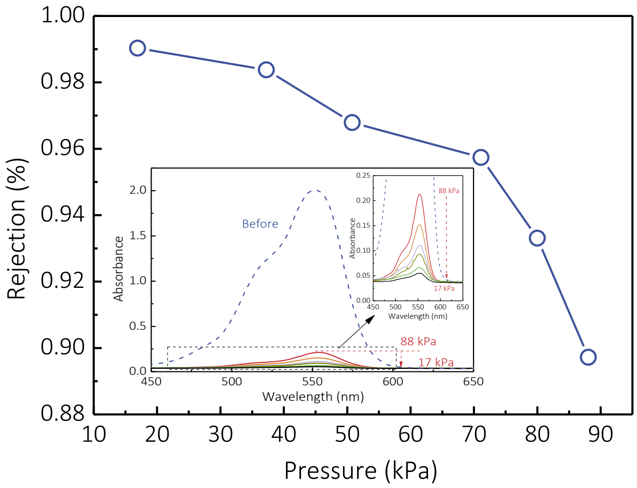

fig. S22. The rejection of 10 ml of 5 µM Rhodamine B aqueous solution for 37-µm-thick SNF/HAP membrane with different applied pressures. The insert plot shows UV-vis absorption changes of an aqueous solution of rhodamine B after filtration with 37 µm thick SNF/HAP membranes with applied pressure.

To evaluate dye adsorption capability of SNF/HAP membranes, the relationship of membrane thickness and dye adsorption capability (**fig. S23**) and the related adsorption equilibrium isotherms (**fig. S24**) were assessed with membranes of different thickness, from 1 to 37 µm. Rhodamine B, Congo Red and Brilliant Blue G were chosen to conduct experiments because these dyes have different molecular sizes, charge and structural features (**Fig. 4g**). The initial concentration and volume of dye in aqueous solutions were set at 150 µM and 40 mL, respectively. In these experiments, the freshly prepared SNF/HAP membranes were directly transferred to dye aqueous solutions and allowed to stand at room temperature for 48 hours to reach adsorption equilibrium. The adsorbed dyes sharply increased when the thickness of membranes was lower than 20 μm and reach equilibrium with increasing thickness. Specifically, a 37-μm-thick membrane adsorbed 2.43 mg Rhodamine B, and theoretically it would have the capability to remove 1L 5 μM Rhodamine B aqueous solution (the concentration used for filtration in our case) even without considering the size-exclusion of membranes.

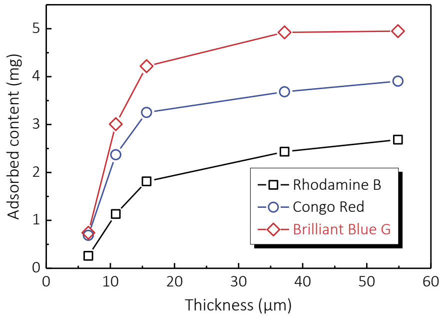

fig. S23. Relationship between membrane thickness and adsorbed dye content.

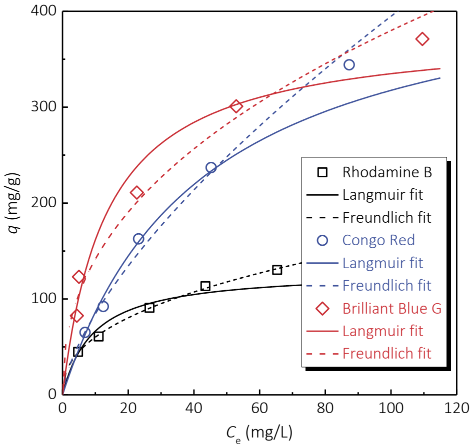

fig. S24. Equilibrium adsorption isotherms of dye adsorption on SNF/HAP membranes.

table S4. Langmuir and Freundlich isotherm parameters of dye adsorption on SNF/HAP nanocomposites.

Adsorbate	Langmuir model			Freundlich model		
	q_m (mg g^{-1})	K_L (L mg^{-1})	R_2	K_F	1/n	R_2
RB	129.4	0.107	0.94	23.04	0.42	0.99
CR	452.5	0.024	0.98	18.07	0.67	0.99
BBG	380.2	0.074	0.90	52.75	0.53	0.94

In order to more quantitatively evaluate the adsorption capacity of the SNF/HAP membranes, the equilibrium data was fitted by Langmuir and Freundlich isotherm models (model details in section S2). **fig. S24** shows the isotherms based on the experimental data, and the parameters obtained from nonlinear regression analysis using adsorption models (**table S4)**. Comparison of the regression coefficients (R^2) of both models showed that the Freundlich isotherm model provided a better fit with the adsorption data. The Freundlich constant, n, in all cases was larger than 1, favorable conditions for adsorption. The maximum adsorption capacity of SNF/HAP membranes for Rhodamine B, Congo Red and Brilliant Blue G are shown in **table S4**, confirming that the SNF/HAP membranes have excellent adsorption for dyes. Interestingly, both the SNF and HAP components are negatively charged at neutral pH and are thus more likely to capture positively charged dyes, but the theoretical maximum adsorption capacity of positively charged Rhodamine B was lower than the negatively charged Congo Red. This difference suggests that other molecular interactions (such as dye-membrane hydrophobic interactions and chemical interaction of dyes) also affect the adsorption equilibrium isotherms.

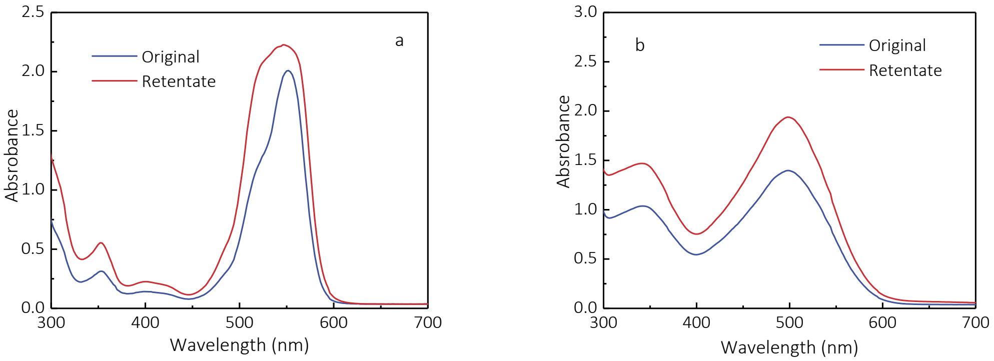

fig. S25. UV-vis spectra of starting and retentate solution of Rhodamine B and Congo Red. The UV-vis spectra of starting and retentate solution of (**a**) Rhodamine B and (**b**) Congo Red. The concentration of Rhodamine B and Congo Red are 5 µM and 17 µM, respectively. The starting volume of dye solutions is 100 mL. The retentate solution is collected after 4 h filtration.

Notably, the maximum adsorption capacity tendency in equilibrium adsorption isotherms is Congo Red > Brilliant Blue G > Rhodamine B, which is different from separation performance recorded by 10 mL filtration experiments as mentioned above, which showed the sequence of Brilliant Blue G (92±1%) > Rhodamine B (84±1%) > Congo Red (67±4%). This finding implies that the size-exclusion affection also contributes to the final separation performance. The UV-vis absorbance of starting and retentate solution of dyes (Rhodamine B and Congo Red) confirmed the results from adsorption isotherms experiments. As shown in **fig. S25**, the retentate solution of both dyes indeed have higher absorbance than the starting solution. Moreover, in our large volume permeate filtration experiments (fig. S26), we used a large amount of Brilliant Blue G aqueous solution (250 mL 398 µM) for filtration and separation. The content of Brilliant Blue G in such solution is much higher than the adsorption capability of a 37-µm-thick membrane, but the rejection remained 100%. This result further confirmed the size exclusion effect of the membranes for filtration experiments. In addition, the continuous feeding separation experiments (Fig. 4g) further confirmed the size-selectivity of SNF/HAP membranes. The 7-µm-thick membranes remain high rejection for most of the dyes even after 24-hour filtration.

To address the stability of the SNF/HAP membranes for large volume permeate filtration, a 250 mL 398 µM Brilliant Blue G aqueous solution and 37-µm-thick membrane were used for separation filtration (**fig. S26**). The solution was allowed to pass through the membrane in 12 h. The SNF/HAP membranes totally rejected all of the dyes even using this large volume permeate. The membrane after filtration was intact and could be easily moved from the filtration device.

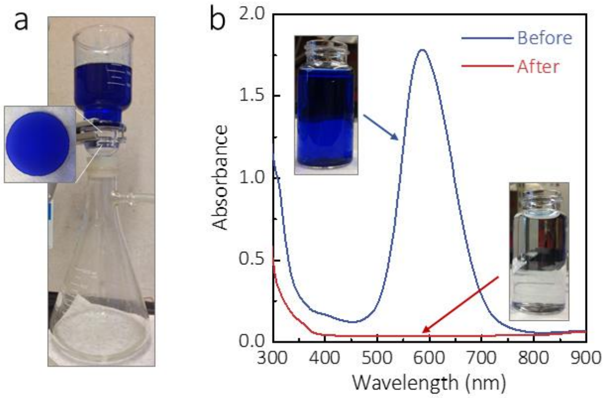

fig. S26. SNF/HAP membrane used for large-volume permeate filtration. (**a**), A photograph of SNF/HAP membrane using for large volume permeate filtration, which successfully rejected Brilliant Blue 8GX. (**b**), UV-vis spectra of Brilliant Blue G aqueous solution collected from before and after filtration.

section S10. Heavy metal ion removal performance of SNF/HAP membranes.

Removing metal ions is a formidable yet critical task for water purification because heavy metal ions tend to accumulate in living organisms and are toxic and cancerogenic (*46*), such as Ni^{2+}, Cr^{3+} and Pb^{2+} (**Fig. 5d**). Therefore, the concentration of metal ions is strictly restricted to trace levels in drinking water. According to the WHO guidelines for drinking water quality (*47*), the concentration of Cu^{2+}, Ni^{2+}, Cr^{3+} and Pb^{2+} should be lower than 2, 0.07, 0.05 and 0.07 mg L^{-1}, respectively (**Fig. 5d**). Previously reported membrane-based technologies have shown advantages for heavy metal removal, such as ease of operation and space saving (*48*), but their removal efficiencies are still poor because the pore sizes of the membranes are larger than the dissolved metal ions. To obtain high efficiency of heavy metal removal, micellar enhanced ultrafiltration and polymer enhanced ultrafiltration have been pursued (*48*); however, both methods were complicated and expensive and resulted in secondary pollution.

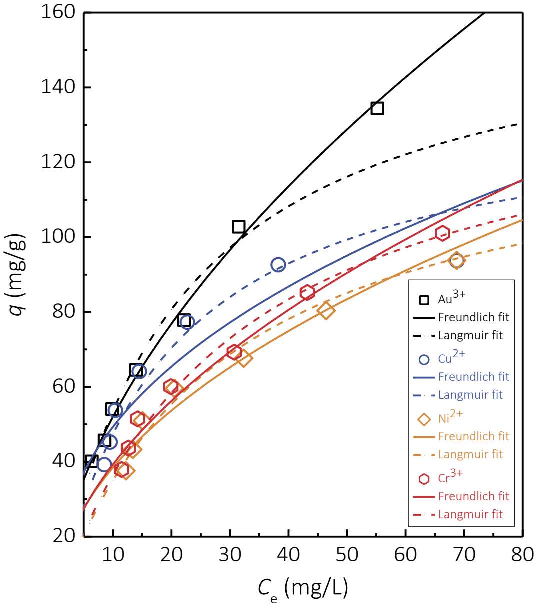

fig. S27. Equilibrium adsorption isotherms of Au^{3+}, Cu^{2+}, Ni^{2+}, and Cr^{3+} adsorption on SNF/HAP nanocomposites. Equilibrium adsorption isotherms of Au^{3+} (a), Cu^{2+} (b), Ni^{2+} (c) and Cr^{3+} (d) adsorption on SNF/HAP nanocomposites.

table S5. Langmuir and Freundlich isotherm parameters of metal ion adsorption on SNF/HAP nanocomposites.

Adsorbate	Langmuir model			Freundlich model		
	q_m (mg g^{-1})	K_L (L mg^{-1})	R_2	K_F	1/n	R_2
Au^{3+}	164.2	0.048	0.98	14.22	0.56	0.99
Cu^{2+}	136.8	0.053	0.93	19.30	0.41	0.85
Ni^{2+}	132.5	0.036	0.95	12.70	0.48	0.94
Cr^{3+}	145.8	0.033	0.96	11.92	0.52	0.96

On the basis of fact that both silk and HAP have been used for removing metal ions (*45*), first, we directly evaluated the adsorption capacity of SNF/HAP multilayer membranes for a series of heavy metal ions (Au^{3+}, Ag^{+}, Cu^{2+}, Ni^{2+}, Pb^{2+} and Cr^{3+}) via a flux-controllable filtration process. Basically, 20 mL 0.2 wt% SNF/HAP solution was used for making the membranes, then 0.01 M metal ion solution was allowed to slowly pass through the SNF/HAP membranes after standing for approximately 4 h. The adsorption capacities of SNF/HAP membranes in this condition for Au^{3+}, Cu^{2+}, Ni^{2+} and Cr^{3+} ions were 135.7, 64.7, 63.0, 126.7 mg g^{-1}, respectively. The adsorption capacity of Ag^{+} and Pb^{2+} are not listed quantitatively because Ag+ and Pb^{2+} interacted with Cl^{-} to yield a precipitate.

According to these initial findings, systematic batch sorption experiments were further designed to evaluate the adsorption performance of Au^{3+}, Cu^{2+}, Ni^{2+} and Cr^{3+} ions on the SNF/HAP adsorbents. First, the 0.2 wt% SNF/HAP solution was concentrated by vacuum filtration to remove most water in solution. The resultant slurry was then processed by freeze-drying to obtain SNF/HAP adsorbents. All the sorption tests were conducted in capped 600 mL flasks containing 150 mL metal ion aqueous solutions, which were prepared with deionized water. The initial metal ion concentration of the adsorption isotherms and kinetic experiments are set as 100 mg L^{-1} and 10 mg L^{-1}, respectively. The dosage of SNF/HAP adsorbents was increased gradually from 50 to 350 mg. After adsorption, the adsorbent was filtered using a 0.2 µm membrane. The residual metal ion concentrations in the solutions were determined by using inductively coupled plasma atomic emission spectrometry (ICP-AES).

fig. S27 shows metal ion sorption isotherms on the SNF/HAP composites. The experimental data are simulated with the Langmuir and Freundlich models (see section 2), respectively. The relative parameters calculated from the two models are listed in **table S5**. It can be seen from **table S5** that both models show good agreement with the experimental data except for Cu^{2+} ion, where the Langmuir model is a better fit than the Freundlich model. The maximum adsorption capacity showed the same tendency with an initial evaluation by using SNF/HAP membranes, that is, $Au^{3+} > Cr^{3+} > Cu^{2+} \approx Ni^{2+}$. Moreover, The Freundlich constant *n* for all ions was larger than 1, which indicates favorable conditions for adsorption.

The adsorption kinetics of metal ions were determined in order to understand the adsorption behavior of the SNF/HAP composites. **fig. S28** and **table S6** show the adsorption data of metal ions by SNF/HAP at different time intervals. The removal rate of metal ion adsorption on SNF/HAP was rapid initially, during the first ~300 min, and then became slow with the increase of contact time from ~300 to ~700 min, and nearly reached a plateau. The time required for Au^{3+}

ion to reach equilibrium was a little longer than that of the other metal ions, which may be attributed to the factor that silk protein can reduce the Au^{3+} ions to Au nanoparticles even under ambient conditions (*65*,*66*). The experimental data was further analyzed by using pseudo-second-order (PS) kinetic models. The R_2 values of the PS kinetic model with least value of 0.92, indicated that the adsorption of metal ions onto SNF/HAP composites followed PS kinetics.

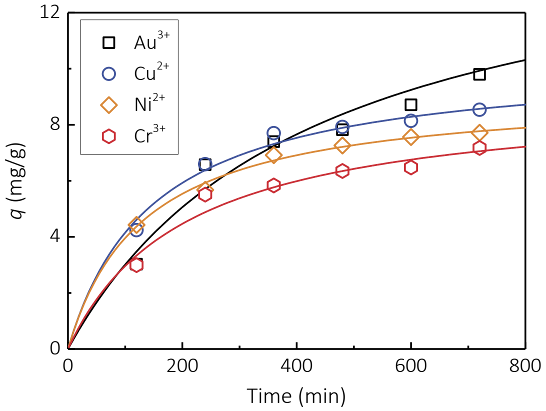

fig. S28. Kinetic curves of SNF/HAP nanocomposites for removing metal ions. The solid lines are fitting results according to second-order adsorption kinetic models.

table S6. Kinetic parameters of second-order adsorption kinetic models for metal ions on SNF/HAP nanocomposites. (Initial metal ions concentration = 10 mg L^{-1})

Adsorbate	q_e (mg g^{-1})	*k*2 (min^{-1})	R^2
Au^{3+}	15.8	1.5×10^4	0.92
Cu^{2+}	10.3	6.5×10^4	0.99
Ni^{2+}	9.2	8.2×10^4	0.99
Cr^{3+}	9.1	5.3×10^4	0.97

section S11. Recycling of metal ion contaminants captured by SNF/HAP membrane via green postprocessing approaches.

The SNF/HAP membranes not only exhibit the excellent adsorption capacity for different metal ions but also provide a new approach to reuse these metal ion contaminants. Au^{3+} ions, for example, we can reuse such noble metal ions through redispersion of SNF/HAP composites. As shown in **fig. S29a**, first, the SNF/HAP membrane after filtering with metal ions (**fig. S29b**) was transferred to water, and then heated at 80°C for 2 or 4 h, the SNF/HAP membrane was broken to several pieces (**fig. S29c**). Next, sonification (120 μm amplitude and 20 KHz frequency, with intervals of 10 sec) was applied to the broken SNF/HAP membrane to obtain SNF/HAP dispersions (**fig. S29d**).

The recycle of metal ion contaminants for the SNF/HAP filtration membranes are summarized in **fig. S30**. For Au^{3+} ions, the Au^{3+} contaminate was used as the source of gold and SNFs served as reductant, no other chemical reagents were needed. The synthesis can be carried out under illumination with sunlight at room temperature or mild heating (~60 °C) (*66*). The Au^{3+} ions were reduced to gold nanoparticles and nanosheets under basic (pH 12) and acidic pH (pH 2) conditions, respectively. The synthetic gold nanoparticles and nanosheets could be collected through syringe filtration or by sedimentation, due to the density difference between gold nanomaterials with the SNF/HAP composites. These gold nanomaterials are useful for bio-imaging, catalysts, and electronics (*67*). Ag^{+} ions, similar to Au^{3+} ions, were directly reduced to Ag nanoparticles under illumination by sunlight at room temperature without chemical reagents (*68*). However, before the filtration to adsorb Ag^{+} ions, the membranes were washed with DI water several times to remove Cl^{-} ions, otherwise, they react with Ag^{+} and generate AgCl particles. The reduced Ag nanoparticles combined with SNF/HAP composites can be assembled to antibacterial membranes (*68*). For Cu^{2+} ions, there are two post-processing methods for reuse: 1, reduce Cu^{2+} ions to Cu nanoparticles by adding $NaBH_4$ solution (*69*); 2, synthesize CuO nanoparticles by adding NaOH solution (*70*). Route 2 was used here as it is more facile and green. The resultant CuO nanoparticles can be used as electrode materials after calcination (*70*). Ni^{2+} ions were reduced to Ni nanoparticles by adding $NaBH_4$ solution (*71*), the resultant Ni nanoparticles showed magnetism and also could be used in magnetic nanomaterials. Cr^{3+} ions can be synthesized to Cr_2O_3 nanoparticles by adding NaOH solution. The Cr_2O_3 nanoparticles are useful dyes in industry. Pb^{2+} ions are more complex to recycle, with a possible approach to preparing PbS nanoparticles by reaction with H_2S gas (*72*), the resultant PbS nanoparticles could be used as catalysts. This reaction was not carried out here. Additional options for green recovery could also include enzymatic digestion of the silk via proteases (*73*) to release the metals or pH related controls for similar goals.

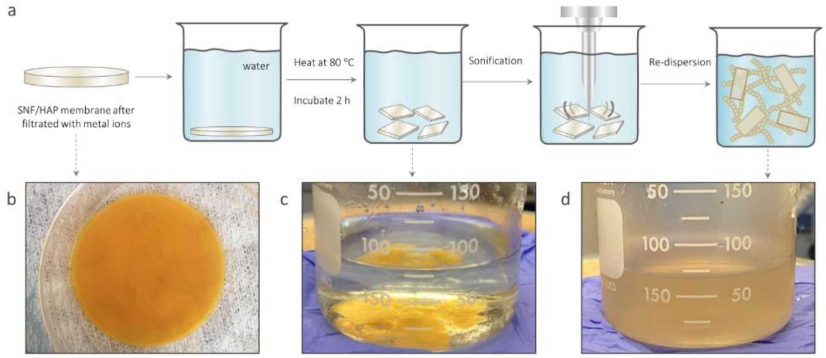

fig. S29. Redispersion of SNF/HAP membranes after filtration with Au^{3+} ions. (**a**) A schematic diagram represents dispersion approach using sonification. (**b-d**) Re-dispersion process of SNF/HAP membrane after filtration with Au^{3+} ion solution. (b) SNF/HAP membrane after filtering with 0.1 M Au^{3+} ion solution. (c) Au^{3+} ion saturated SNF/HAP membrane after incubation in 80 mL water at 80°C for 4 h. 4) The SNF/HAP dispersion prepared from solution (c) after sonification at 120 µm amplitude and 20 kHz frequency, with intervals of 10 sec for 1 h.

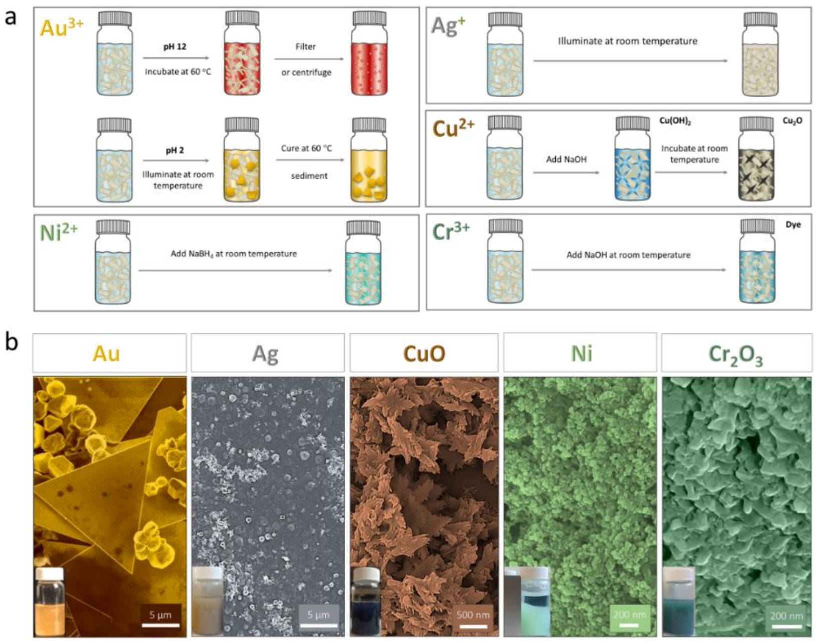

fig. S30. Recycling of metal ion contaminants via green postprocessing approaches. (**a**) The schematics of post-processing methods for specific metal ion contaminants. The useful metal nanomaterials were directly synthesized from ions/SNF/HAP dispersions (first column images) that were prepared from an ultrasonic dispersion of adsorbed-saturated ion SNF/HAP membranes. The limiting adsorption ability of SNF/HAP composites is larger than SNF/HAP membranes. Thus, to achieve maximum reduction of metal ions, 1 mL 0.1 M metal ions were added into 10 g re-dispersed SNF/HAP dispersion to absorb more metal ions followed by reduction with specific methods. (**b**) The metal nanomaterials synthesized from metal ion contaminants by using post-processing approaches. The detailed post-processing methods were showed in (a). For Au^{3+} ions, gold nanosheets are shown, which were reduced by SNFs under sunlight at pH 2. The reduced gold nanoparticles were shown in Fig. 5e.

section S12. Comparing the costs and maximum sorption capacities of SNF/HAP membranes with other nanoadsorbents.

table S7. Estimated total cost for preparing 1 g of nanoadsorbents.

Adsorbent	Used materials and chemicals	Amount used	Unit cost US $	Cost US$	Total chemical and material cost (US $ per gram of adsorbent	Other costs increasing factors or remarks	Reference
Hematite (α-Fe_2O_3)	$FeCl_3$	2.7 g	6.52	17.60	**21.75**	Heating at 90 °C for 2 days	(*74*)
	DI water	500 mL	0.0226	11.3			
	HCl	0.05 mL	0.549	0.03			
γ-Fe_2O_3	DI water	200 mL	0.0226	4.52	**19.01**	Nitrogen gas, rinsed ultrapure water, freeze-drying	(*75,76*)
	$FeCl_3$	5.2 g	6.52	33.90			
	$FeCl_2$	2.0 g	3.18	6.36			
	NH_4OH	1.5 M	0.0826	2.90			
	Tetramethylammonium hydroxide	1 mL 25%	0.2264	0.23			
	99% Octyl ether	N/A	N/A				
α-MnO_2 (OMS-2)	$NaSO_4$	250 mL 0.15 M	0.1042	0.56	**10.35**	Heating and boiling for 24 h, ion-exchanged water	(*77*)
	DI water	250 mL	0.0226	5.65			
	65% HNO_3	11.5 mL	0.41	2.46			
	$KMnO_4$	2.1 g	1.592	3.34			
α-MnO_2 (OMS-1)	$MnSO_4$	400 mL C_{Mn2+}=0.6 M	0.273	11.07	**1.84**	Nitrogen gas, oxygen, DI water for washing	(*78,79*)
	NaOH	400 mL 5 M	0.1886	15.09			
	$MgCl_2$	1 M	0.537	12.24			
γ-MPTMS modified γ-Al_2O_3	Al_2O_3	5 g	9.175	45.88	**21.00**	DI water and ethanol for washing, vacuum drying	(*80*)
	Benzene	100 mL	0.595	59.50			
	R-MPTMS	1% (m/v)	1.224	1.22			
DNPH modified γ-Al_2O_3	Alumina nanoparticles	2.0 g	9.175	18.35	**10.53**		(*81*)
	DI water	50 mL	0.0226	1.13			
	SDS	0.1 g	1.62	0.16			
	2,4-dinitrophenylhydrazine (0.90 g DNPH in HCl + acetonitrile)	0.9	1.572	1.41			
ZnO	$Zn(CH_3COO)_2$•$2H_2O$	0.66 g	12.88	8.50	**83.12**	Heating at 160 °C for 12 h, DI water and ethanol for washing	(*82*)
	Urea	0.54 g	0.1542	0.08			
	Ethylene glycol	25 mL	0.432	10.80			
	DI water	25 mL	0.0226	0.57			
CeO_2	$Ce(NO_3)_3 \cdot 6H_2O$	100 mL 1mM	9.66	4.19	**37.60**	Autoclave, heating at 500 °C for 2 h	(*83*)
	Urea	1.5 mmol	0.1542	0.01			
	DI water	100 mL	0.0226	2.26			
TEMPO oxided CNC	CNC	1 g	0.3	0.30	**2.80**	Dialyzing cellulose dialysis membrane for 1 week	(*84*)
	TEMPO-reagent	0.059 g	0.57	0.33			
	NaBr	0.325 g	0.112	0.04			
	NaClO	7.1 mL	0.190	1.35			
	Methanol	11 mL	0.063	0.70			
	NaOH	N/A mL	0.008	N/A			
	HCl	N/A mL	0.01	N/A			
Succinic anhydride/CNC	CNC powder	1 g	0.17	0.17	**0.65**	Drying in vacuum at 383 K for 24 h	(*84*)
	N,N-dimethylacetamide	5 mL	0.063	0.32			
	Succinic anhydride	0.6 g	0.26	0.16			
	Sodium hydrogencarbonate	N/A g	0.018	N/A			
MWCNT	/	/	/	/	**42.35**		Sigma-Aldrich
SWCNT	/	/	/	/	**676**		Sigma-Aldrich
MWCNT, carboxylic acid functionalized	/	/	/	/	**116.5**		Sigma-Aldrich
Graphene oxide	/	/	/	/	**2215**		Sigma-Aldrich
SNF/HAP	Cocoons	1 g	0.015	0.02	**3.36**	Degumming and dialysis	**Current work**
	LiBr	8.077 g	0.120	0.97			
	DI water	100 mL	0.023	2.26			
	$CaCl_2$	0.133 g	0.343	0.05			
	Na_2HPO_4	0.17 g	0.39	0.07			

The prices of chemical reagents, carbon nanotubes, and graphene oxide were obtained from Sigma-Aldrich website (https://www.sigmaaldrich.com/united-states.html). The price of cocoons was obtained from Alibaba website (https://www.1688.com/). The price of cocoons has some differences, depending on the place of purchase and the type of cocoons. Here a chose a median price to the calculation. The cost of SNF/HAP can be further reduced if using industrial waste silk as raw materials. Abbreviations: DI water, deionized water; OMS, octahedral molecular sieves; γ-MPTMS, γ-mercaptopropyltrimethoxysilane; DNPH, 2,4-Dinitrophenylhydrazine; SDS, sodium dodecyl sulfate; CNC, cellulose nanocrystals; TEMPO, 2,2,6,6-tetramethylpiperidinyl-1-oxyl radical; CNT, carbon nanotube; MCNT, multi-wall carbon nanotube; SWCNT, single-wall carbon nanotube; SNF, silk nanofibrils; HAP, hydroxyapatite.

table S8. Maximum sorption capacities of metal ions with different nanomaterials.

Adsorbent	Preparation	Conditions	Target metals	Maximum sorption capacity (mg/g)	Reference
Hematite (α-Fe_2O_3)	Coprecipitation	pH=5.2±0.1	Cu^{2+}	84.46	(*74*)
γ-Fe_2O_3	Sol-gel method	pH=2-3	Cr^{4+}	19.2	(*75*)
		pH=2.5	Cr^{4+}	17.0	(*76*)
		pH=6.5	Cu^{2+}	26.8	(*76*)
		pH=8.5	Ni^{2+}	23.6	(*76*)
α-MnO_2 (OMS-2)	Precipitation method		Cu^{2+}	83.2	(*77,78*)
α-MnO_2 (OMS-1)	Precipitation method		Cu^{2+}	57.6	(*78*)
γ-MPTMS modified γ-Al_2O_3	Mixture		Cu^{2+}	Removal 100%	(*80*)
			Hg^{2+}	Removal 97.8-99%	(*80*)
			Pd^{2+}	Removal 97-100%	(*80*)
DNPH modified γ-Al_2O_3	Chemically immobilization		Pb^{2+}	100	(*81*)
			Cd^{2+}	83.33	(*81*)
			Cr^{4+}	100	(*81*)
			Co^{2+}	41.66	(*81*)
			Ni^{2+}	18.18	(*81*)
			Mn^{2+}	6.289	(*81*)
ZnO	Hydrothermal		Pb^{2+}	6.7	(*82*)
CeO_2	Precipitation		Cr^{4+}	15.4	(*83*)
			Pb^{2+}	9.2	(*83*)
CNC	Succinic anhydride	pH=5.6	Pb^{2+}	465.75	(*85*)
	(Carboxyl)	pH=6	Cd^{2+}	343.84	(*86*)
			Zn^{2+}	104	(*86*)
			Ni^{2+}	43.66	(*86*)
			Cu^{2+}	121.6	(*86*)
			Co^{2+}	79.08	(*86*)
			Cd^{2+}	231.5	(*86*)
CNC	TEMPO-oxidized		Cu^{2+}	268.2	(*87*)
			Cs^{+}	133.8	(*87*)
			Zn^{2+}	~195	(*87*)
			Cd^{2+}	~118	(*87*)
			Fe^{2+}	~95	(*87*)
			Ca^{2+}	~64	(*88*)
			Cu^{2+}	~90	(*88*)
			Ag^{+}	~202	(*88*)
			Pb^{2+}	~387	(*88*)
CNT		pH=7.0	Pb^{2+}	1.0	(*89*)
		pH=5.0	Pb^{2+}	102.04	(*90*)
			Cd^{2+}	1.1	(*91*)
CNT	HNO_3 treatment		Pb^{2+}	49.95	(*89*)
			Cd^{2+}	5.1	(*91*)
		pH=5.0	Pb^{2+}	35.6	(*92*)
CNT	H_2O_2 treatment	pH=5.5	Cd^{2+}	2.6	(*91*)
CNT	$KMnO_4$ treatment	pH=5.5	Cd^{2+}	11.0	(*91*)
MCNT	HNO_3 treatment		Cd^{2+}	7.42	(*93*)
			Ni^{2+}	6.89	(*93*)
		pH=5.0	Cd^{2+}	10.86	(*94*)
		pH=5.0	Cu^{2+}	24.49	(*94*)
		pH=5.0	Pb^{2+}	97.08	(*94*)
		pH=6.55	Ni^{2+}	9.8	(*95*)
SWCNT		pH=7.0	Ni^{2+}	9.22	(*96*)
			Zn^{2+}	11.23	(*97*)
SWCNT	NaOCl treatment		Ni^{2+}	47.85	(*96*)
			Zn^{2+}	43.66	(*97*)
MWCNT			Ni^{2+}	7.53	(*96*)
			Zn^{2+}	10.21	(*97*)
MWCNT	NaOCl treatment		Ni^{2+}	38.46	(*96*)
			Zn^{2+}	32.68	(*97*)
MWCNT	Iron oxide		Ni^{2+}	9.18	(*98*)
Acidified MWCNT			Pb^{2+}	85	(*99*)
Graphene oxide	Modified Hummers method	pH=6.0; T=303 K	Cd^{2+}	106.6	(*100*)
		pH=6.0; T=313 K	Cd^{2+}	153.6	(*100*)
		pH=6.0; T=333 K	Cd^{2+}	167.5	(*100*)
		pH=6.0; T=303 K	Co^{2+}	68.2	(*100*)
		pH=6.0; T=313 K	Co^{2+}	69.4	(*100*)
		pH=6.0; T=333 K	Co^{2+}	79.8	(*100*)
		pH=4.68	Cu^{2+}	62.73	(*101*)

Abbreviations: OMS, octahedral molecular sieves; γ-MPTMS, γ-mercaptopropyltrimethoxysilane; DNPH, 2,4-Dinitrophenylhydrazine; CNC, cellulose nanocrystals; TEMPO, 2,2,6,6-tetramethylpiperidinyl-1-oxyl radical; CNT, carbon nanotube; MCNT, multi-wall carbon nanotube; SWCNT, single-wall carbon nanotube